Journal Name

ARTICLE

Electronic Supporting Information (*ESI*) for

High-Performance Solar Vapor Generation by Sustainable Biomimetic Snake-Scale-Like Porous Carbon

Ning Liu, Liang Hao, Boyi Zhang, Ran Niu, Jiang Gong* and Tao Tang*

Table S1 The S_{BET}, evaporation rate, solar-to-vapor conversion efficiency, and enhancement factor of BSPC-*x*.

Sample	S_{BET} (m^2/g)	Evaporation rate ($kg/m^2/h$)	Efficiency (%)	Enhancement factor
BSPC-0	371.1	0.77	38	1.31
BSPC-0.5	547.9	1.02	55	1.65
BSPC-1	662.2	1.26	70	2.03
BSPC-2	732.3	1.58	91	2.53
W-BSPC-2	710.4	1.54	89	2.48

Table S2 Summary of solar steam generation performance of some previously reported photothermal materials under 1 kW/m^2.

Entry	Photothermal material	Evaporation rate ($kg/m^2/h$)	Efficiency (%)	Reference in *ESI*
1	BSPC-2	1.58	91	This work
2	Au NR/NP	1.18	76	[S1]
3	Plasmonic wood	1.00	68	[S2]
4	Au film	1.00	64	[S3]
5	Black gold membrane	0.67	42	[S4]
6	Geopolymer-biomass carbon composite	1.58	85	[S5]
7	Porous N-doped graphene	1.50	80	[S6]
8	GO/cellulose/PS	1.45	80	[S7]
9	Carbonized longitudinal wood	1.08	74	[S8]
10	F-wood	1.05	72	[S9]
11	Carbonized polyurethane sponge	1.05	51	[S10]
12	F-wood/CNTs	0.95	65	[S11]
13	rGO/cellulose esters	0.84	60	[S12]
14	GO-SA-CNT aerogel	0.50	40	[S13]
15	rGO membrane	0.47	48	[S14]
16	Multilayer PPy	1.38	92	[S15]
17	PPy/stainless steel	0.92	58	[S16]

18	PDA-sponge	1.18	92.1	[S17]
19	Hollow melamine foam/reduced graphene oxide composite	1.476	92.9	[S18]
20	Poly(ionic liquid)-derived porous carbon membrane	1.19	74.69	[S19]

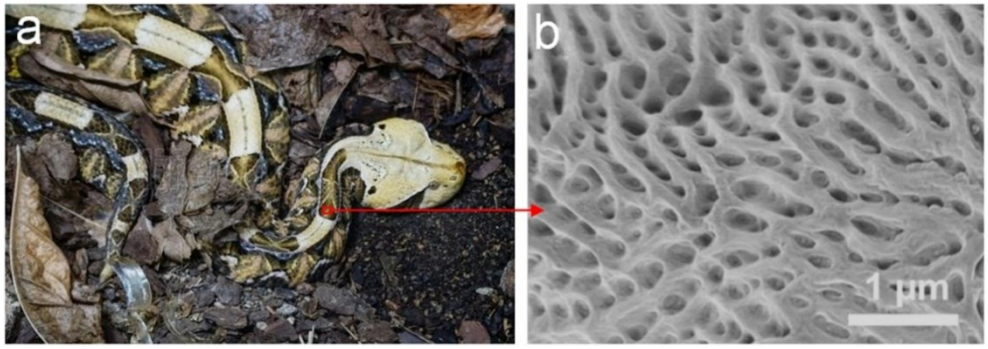

Fig. S1 (a) Photograph of a West African Gaboon viper surrounded by leaves. (b) SEM image of West African Gaboon viper's scales according to the previous work [S20]. Note: West African Gaboon viper shows black spots on dorsal scales with geometrically patterned surface texture.

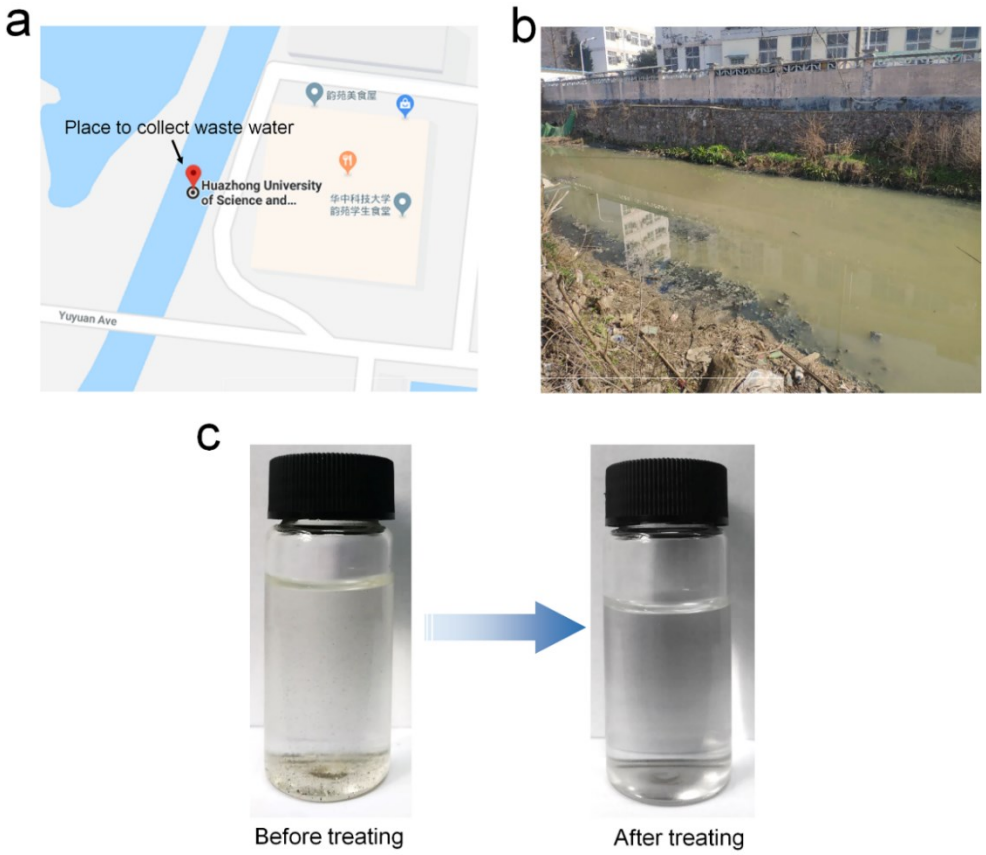

Fig. S2 (a) The location and (b) photograph of the place to collect life wastewater from Huxi River in the campus of Huazhong University of Science and Technology (Wuhan, China). (c) Photographs of the wastewater and the condensed water by using BSPC-2.

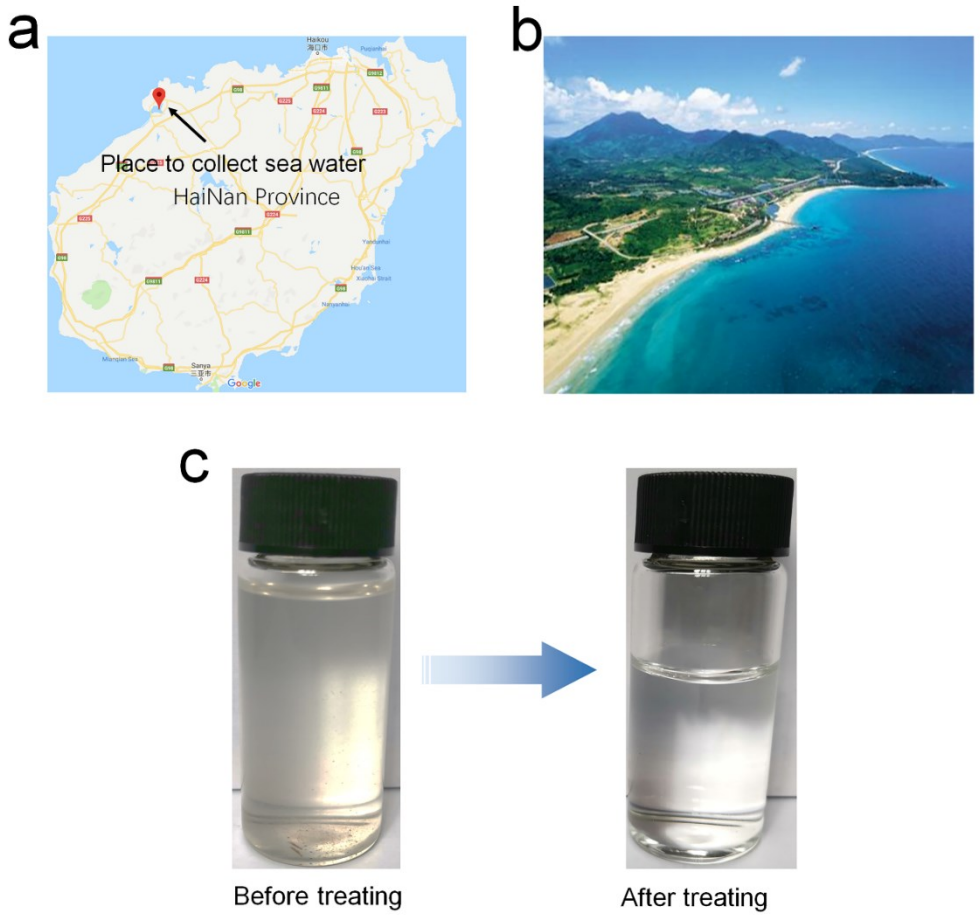

Fig. S3 (a) The location and (b) photograph of the place to collect seawater from South Sea (near to Danzhou, Hainan, China). (c) Photographs of the seawater and the condensed water by using BSPC-2.

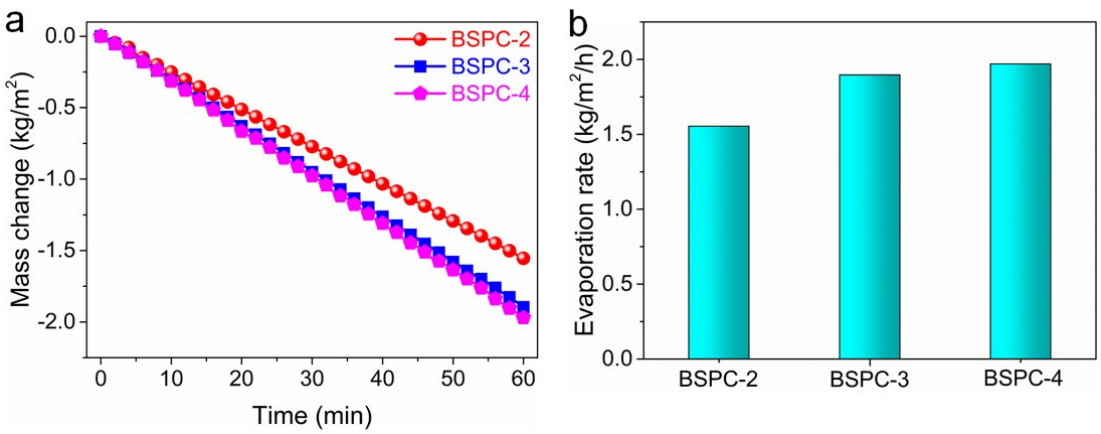

Fig. S4 (a) The cumulative water mass changes over irradiation time and (b) the evaporation rates of BSPC-2, 3 and 4 membranes.

Note: the evaporation rate of BSPC-3 or BSPC-4 indeed is slightly higher than that of BSPC-2. However, compared to BSPC-2, greatly more amounts of ZnO and HCl solution are consumed in preparing BSPC-3 or BSPC-4. Besides, the yields of BSPC-3 and BSPC-4 (i.e., 15.0% and 13.6%, respectively) are greatly lower than that of BSPC-2 (23.8 wt%). Thereby, the highest ZnO/PET mass ratio is selected as 2 in this work.

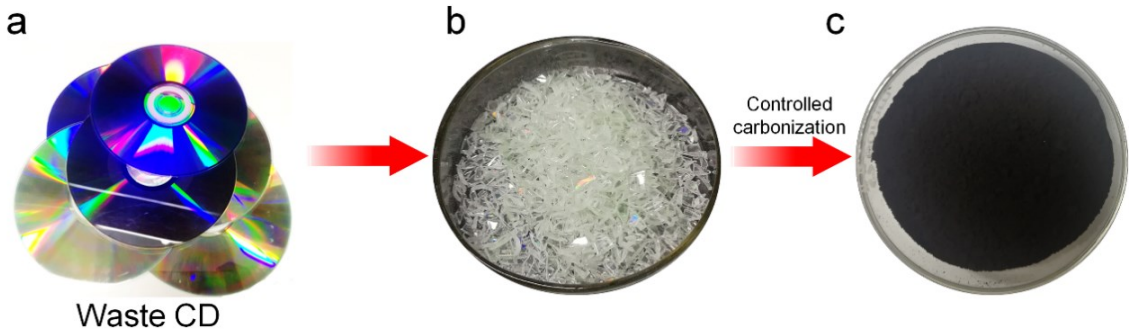

Fig. S5 Photographs of (a) waste CD, (b) PC pieces obtained from waste PC, and (c) the as-prepared W-BSPC-2 from carbonization of PC waste catalyzed by ZnO at 550 ^{o}C.

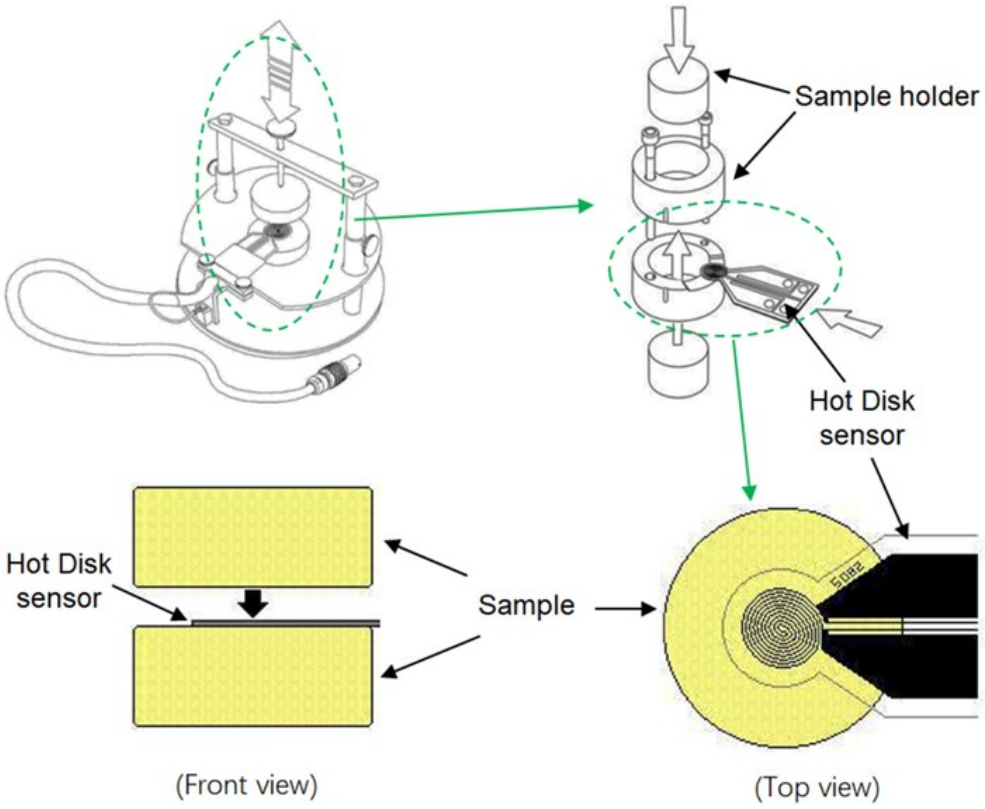

Fig. S6 Scheme for measuring thermal conductivity of BSPC-2 in Shiyanjia Lab.

Measurement method: When measuring a powder sample, the Hot Disk probe needs to be placed inside the sample so that it remains flat during transient recording. In addition, the mechanical pressure can be easily controlled by using the sample gripper.

Calculation method (Transient Plane Source Method): During the test, the probe is placed in the middle for the test. When the current passes through nickel (some probes are made of nickel), it produces a certain temperature rise, and the heat generated simultaneously diffuses to the sample on both sides of the probe depending on the thermal conduction characteristics of the material. By recording the temperature and probe response time, the thermal conductivity and thermal diffusion rate can be directly obtained through the mathematical model.

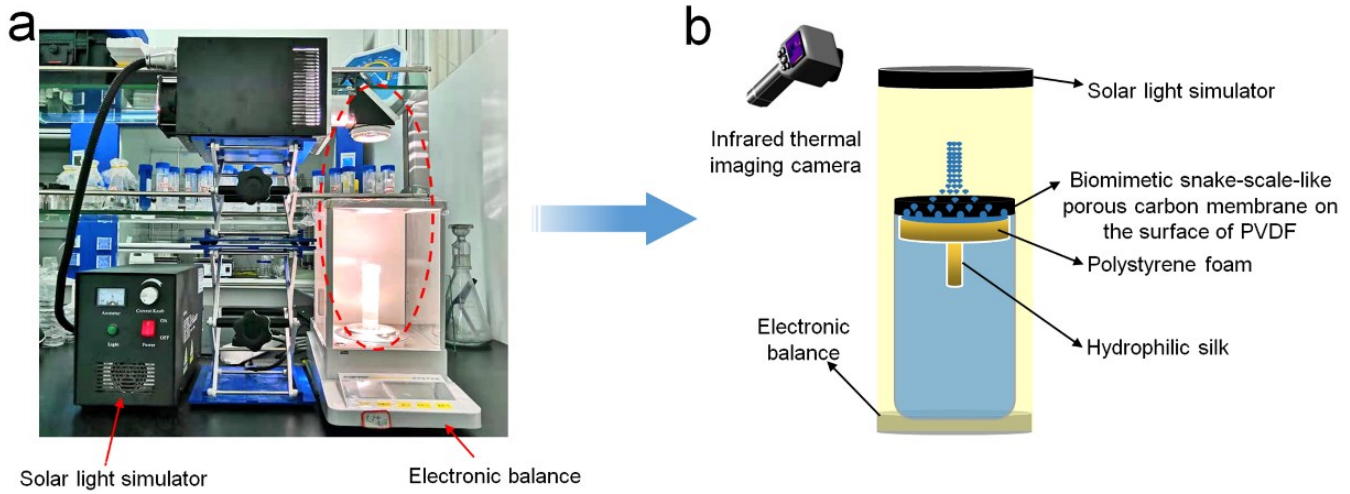

Fig. S7 (a) Photograph and (b) schematic illustration of the interfacial solar-driven steam generation instrument used in this work.

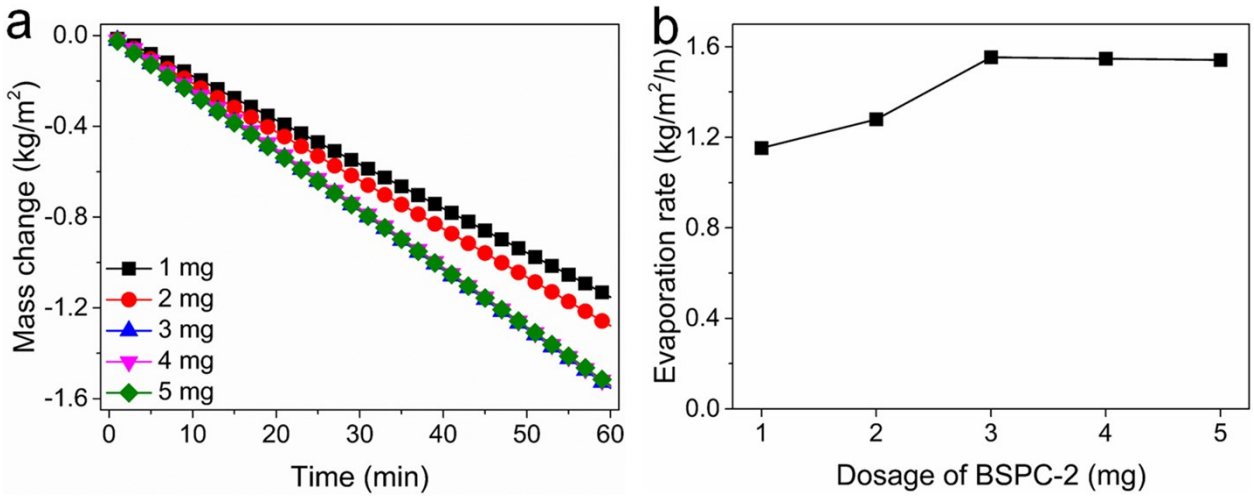

Fig. S8 Effect of BSPC-2 dosage on (a) the cumulative water mass change over irradiation time and (b) the evaporation rate of BSPC-2 membrane.

Note: when the BSPC-2 dosage increases from 1 mg to 2 or 3 mg, the evaporation rate of BSPC-2 membrane goes up from 1.15 kg/m^2/h to 1.28 or 1.58 kg/m^2/h. However, when the BSPC-2 dosage further raises to 4 or 5 mg, the evaporation rate of BSPC-2 membrane seems stagnating.

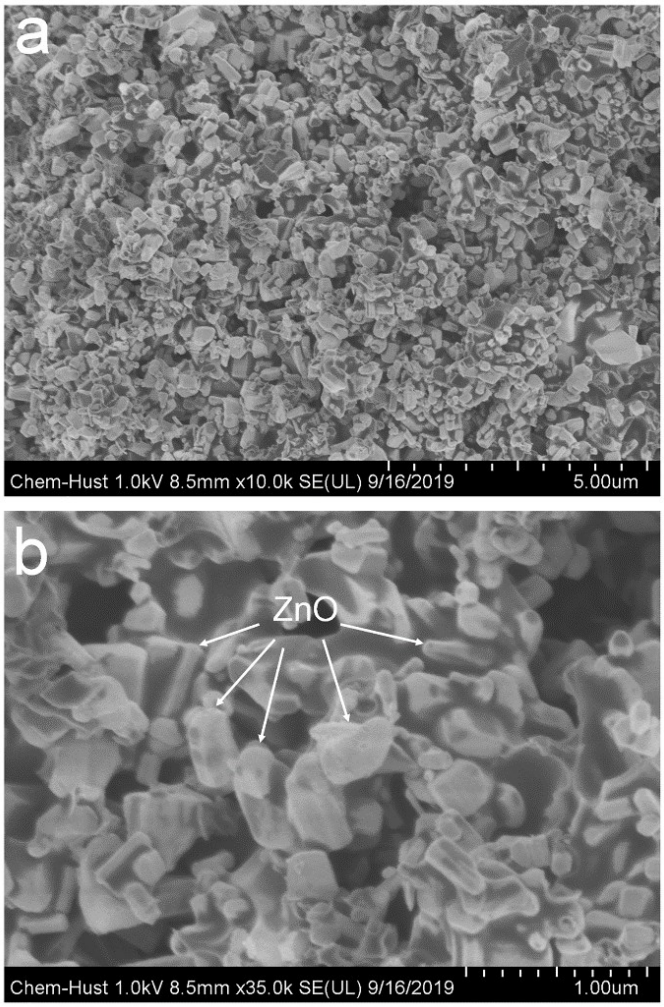

Fig. S9 SEM images in (a) low and (b) high magnification of BSPC-2/ZnO composite before the removal of ZnO.

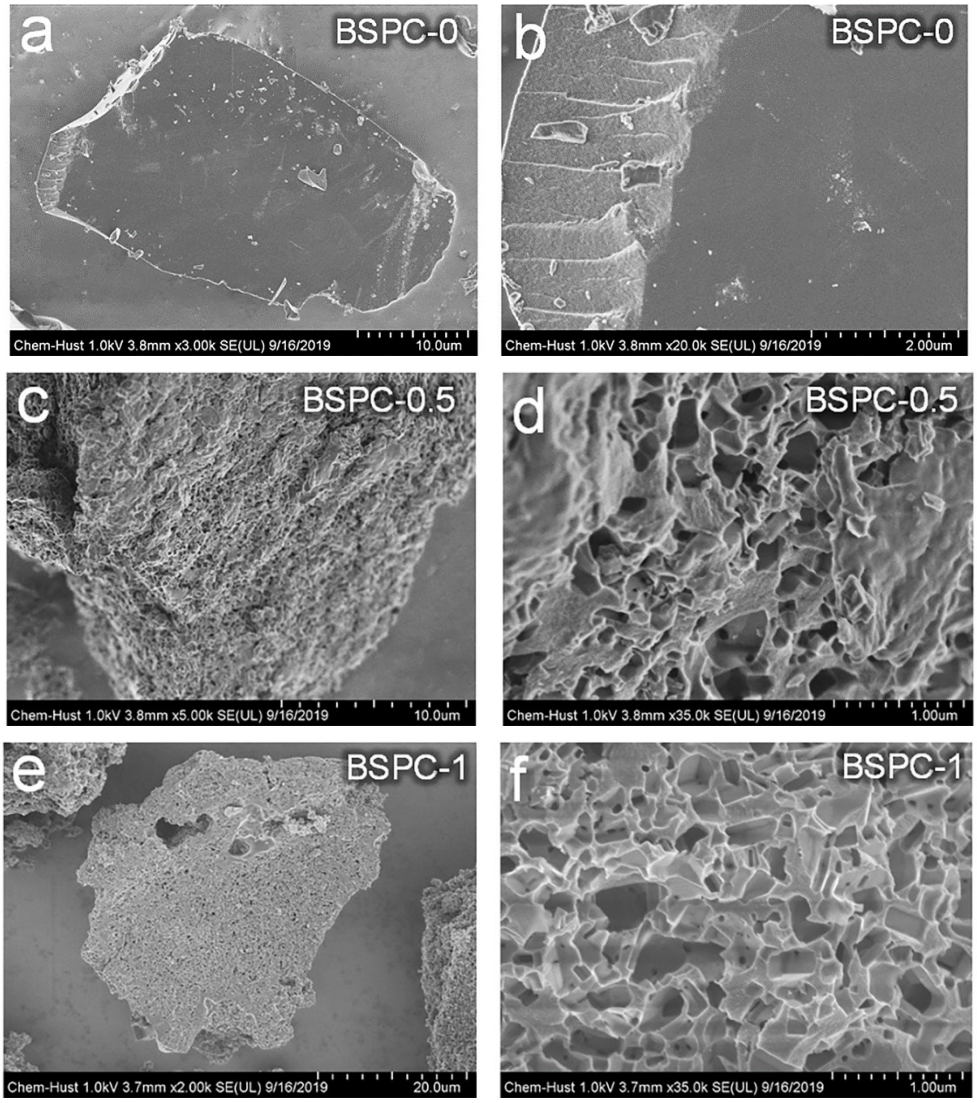

Fig. S10 SEM images of (a and b) BSPC-0, (c and d) BSPC-0.5, and (e and f) BSPC-1.

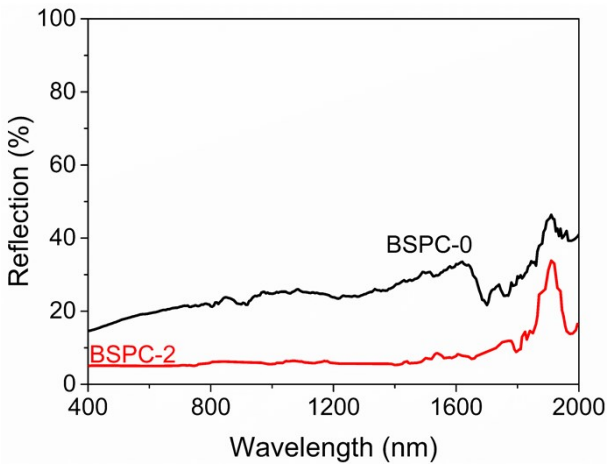

Fig. S11 Comparison of light reflection between BSPC-0 and BSPC-2 membranes.

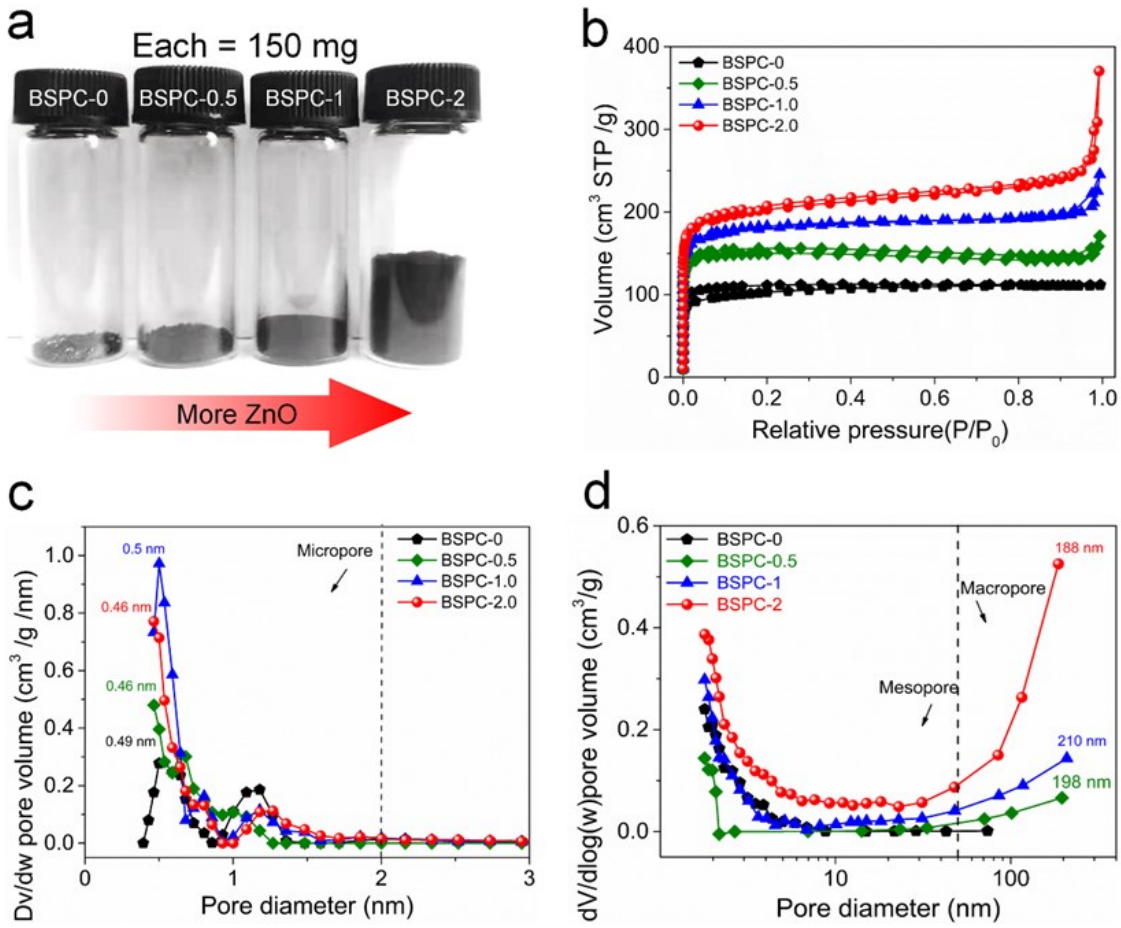

Fig. S12 (a) Photographs of BSPC-*x* from PC by using a different amount of ZnO at 550 °C. (b) N_2 adsorption/desorption isotherms of BSPC-*x* at 77 K. Pore size distribution plots of BSPC-*x* using (c) DFT or (d) BJH model.

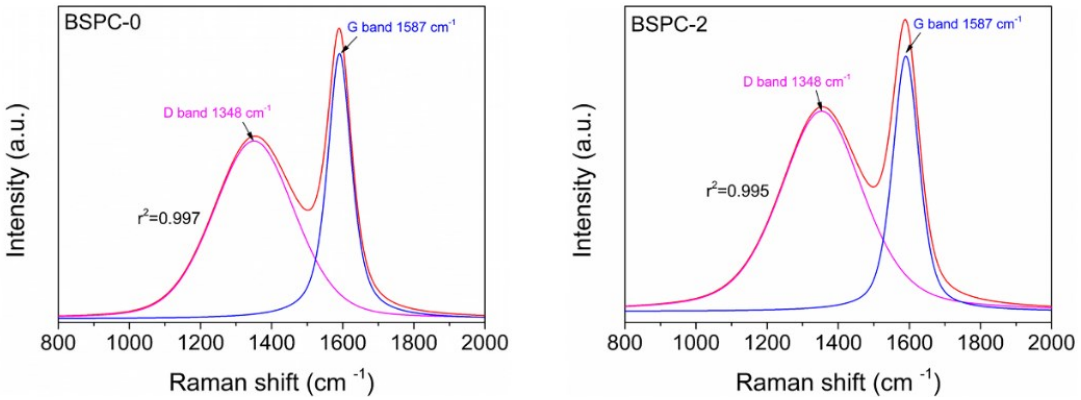

Fig. S13 The fitting results of Raman spectra of (a) BSPC-0 and (b) BSPC-2 using the PeakFit.

Fig. S14 Schematic illustration of ZnO recycling.

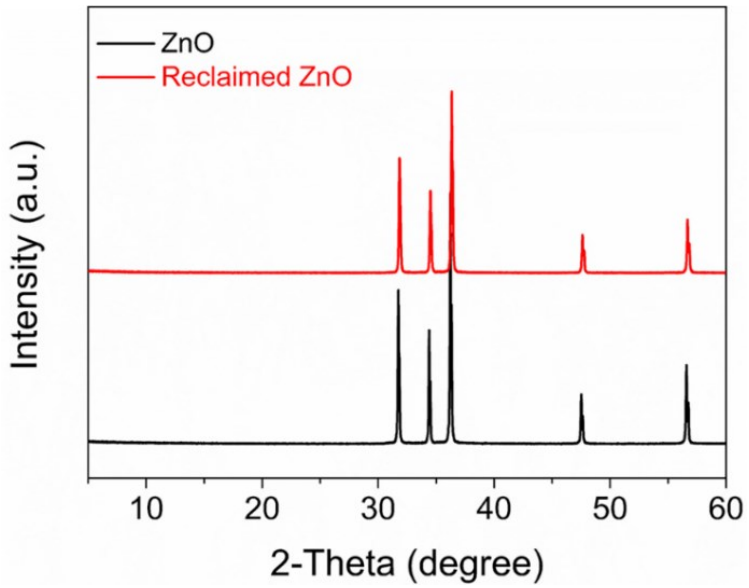

Fig. S15 XRD patterns of the original and reclaimed ZnO catalysts.

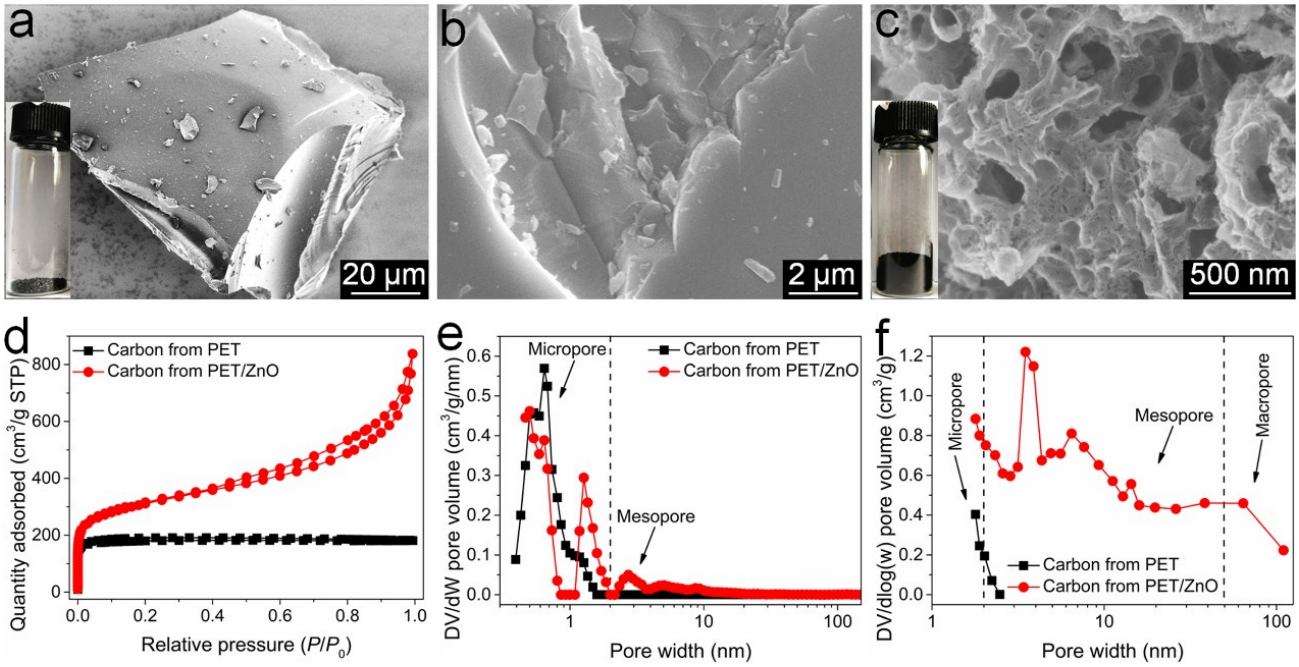

Fig. S16 SEM images of carbon product from (a and b) PET or (c) PET/ZnO mixture; the insets in (a) or (c) show the photos of the corresponding samples with the mass of 500 mg. (d) N_2 adsorption/desorption isotherms and pore size distribution plots using (e) DFT model or (f) BJH model of carbon product from PET or PET/ZnO mixture.

Note: in the absence of ZnO, the carbon product from PET consists of smooth-surfaced particles with a size of 20–100 μm, while the carbon product from PET/ZnO mixture bear obviously rough surface and porous structure, similar with BSPC-2. Besides, the carbon product from PET bears mainly micropores with S_{BET} of 650 m^2/g. By contrast, the carbon product from PET/ZnO mixture exhibits hierarchical micropores, mesopores and macropores with S_{BET} of 1163 m^2/g. As we can see, ZnO works well in the controlled carbonization of PET into hierarchically porous carbon. More detailed results will be reported in our future work.

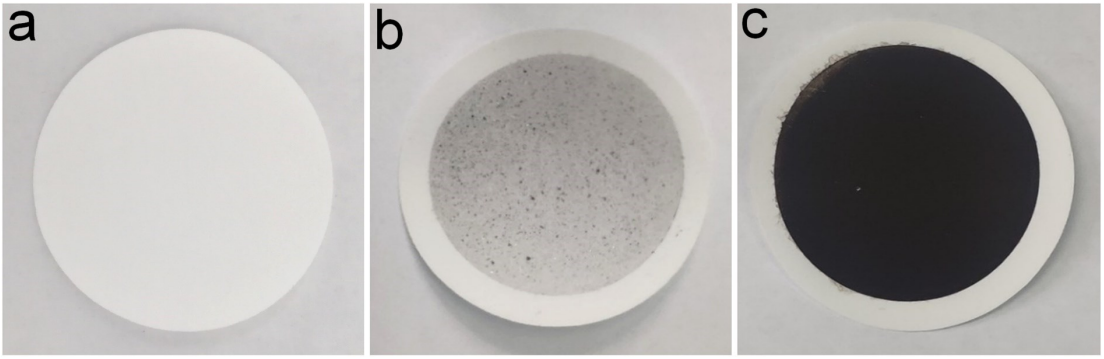

Fig. S17 Photographs of (a) PVDF matrix membrane, (b) BSPC-0 membrane and (c) BSPC-2 membrane.

Note: the packing density of BSPC-0 is relatively high. During the preparation of membrane, the dosage of photothermal materials (e.g., 3 mg) is fixed. In this regard, the coverage of carbon particles in the BSPC-0 membrane is very low, which seems similar with that of PVDF matrix membrane but greatly less than that of BSPC-2 membrane. Such low coverage of carbon particles in BSPC-0 membrane could not reflect fully the role of nanopores in water transportation and light adsorption. Thereby, compared to the matrix PVDF membrane (0.72 $kg/m^2/h$), the evaporation rate of BSPC-0 membrane (0.78 $kg/m^2/h$) does not show a significant improvement.

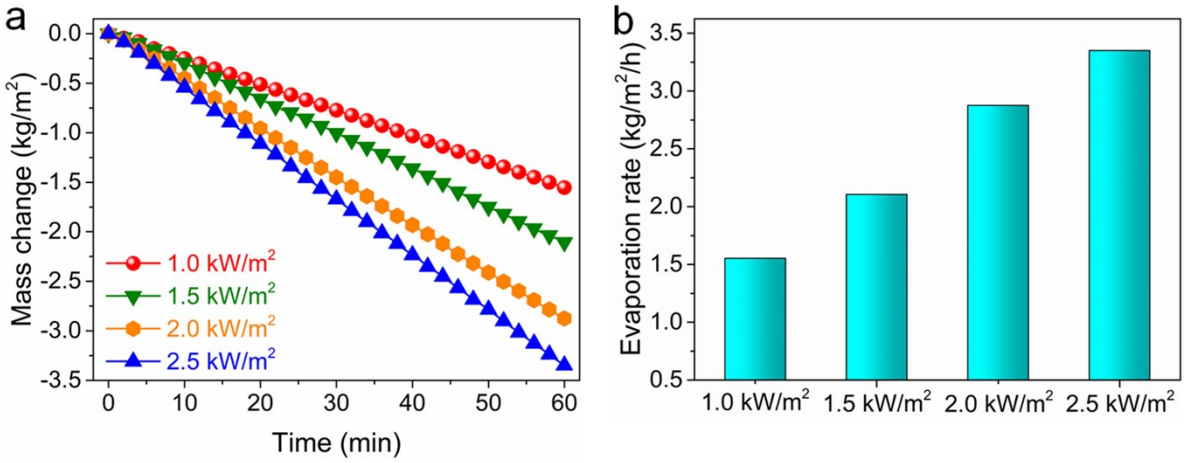

Fig. S18 Effect of the irradiation intensity on (a) the cumulative water mass change over irradiation time and (b) the evaporation rate of BSPC-2 membrane.

Note: when the irradiation intensity increases from 1 kW/m² to 1.5, 2.0 and 2.5 kW/m², the evaporation rate of BSPC-2 goes up from 1.58 kg/m²/h to 2.11, 2.88 and 3.35 kg/m²/h, respectively.

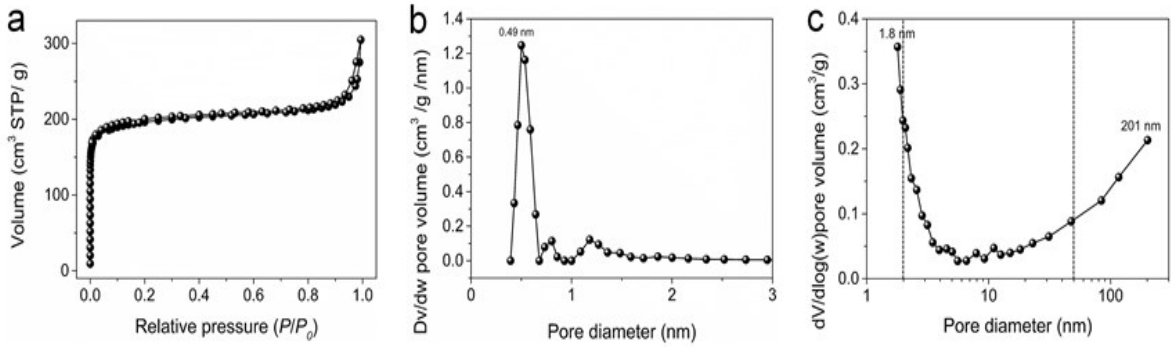

Fig. S19 (a) N_2 adsorption/desorption isotherms of W-BSPC-2 at 77 K. Pore size distribution plots of W-BSPC-2 using (b) DFT model or (c) BJH model.

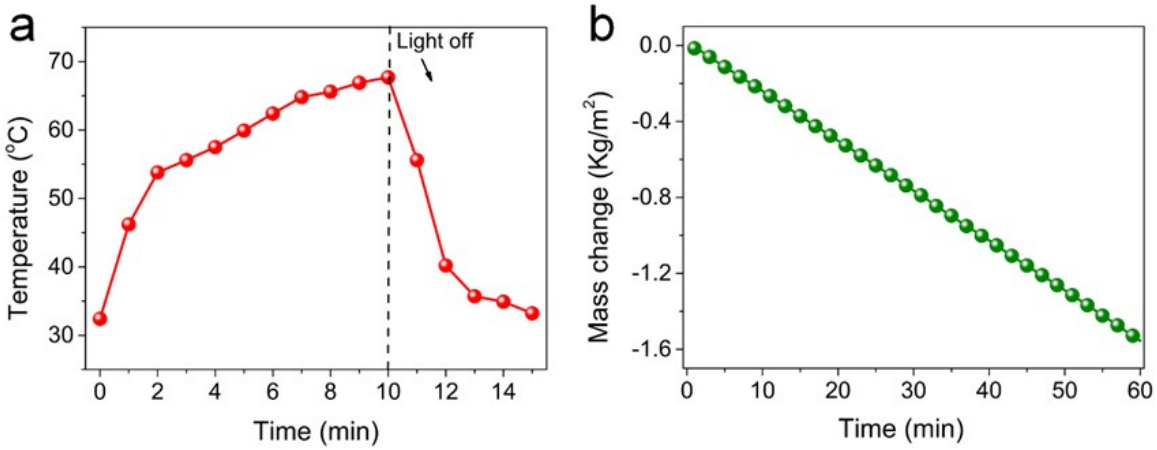

Fig. S20 (a) Surface temperature of W-BSPC-2 under 1 kW/m² solar light irradiation over different time, and (b) cumulative mass change of water using W-BSPC-2 over different time.

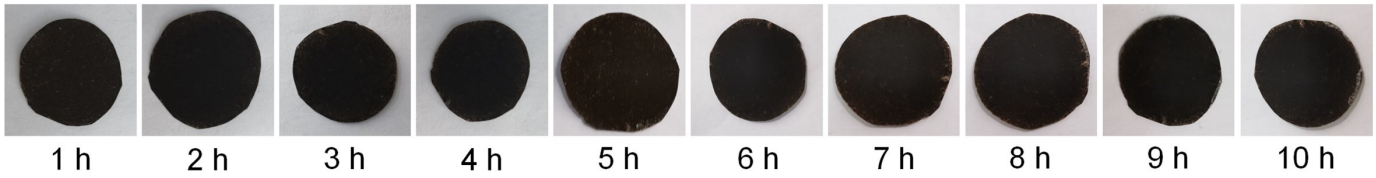

Fig. S21 Photographs of BSPC-2 membrane during the seawater solar steam generation.

Reference in *ESI*

[S1] F. J. Tao, Y. L. Zhang, K. Yin, S. J. Cao, X. T. Chang, Y. H. Lei, D. S. Wang, R. H. Fan, L. H. Dong, Y. S. Yin, X. B. Chen, Copper sulfide-based plasmonic photothermal membrane for high-efficiency solar vapor generation, ACS Appl. Mater. Interfaces 10 (2018) 35154-35163.

[S2] M. Zhu, Y. Li, F. Chen, X. Zhu, J. Dai, Y. Li, Z. Yang, X. Yan, J. Song, Y. Wang, E. Hitz, W. Luo, M. Lu, B. Yang, L. Hu, Plasmonic wood for high-efficiency solar steam generation, Adv. Energy Mater. 8 (2018) 1701028.

[S3] L. Zhou, Y. Tan, D. Ji, B. Zhu, P. Zhang, J. Xu, Q. Gan, Z. Yu, J. Zhu, Self-assembly of highly efficient, broadband plasmonic absorbers for solar steam generation, Sci. Adv. 2 (2016) 1501227.

[S4] K. Bae, G. Kang, S. K. Cho, W. Park, K. Kim, W. J. Padilla, Flexible thin-film black gold membranes with ultrabroadband plasmonic nanofocusing for efficient solar vapour generation, Nat. Commun. 6 (2015) 10103.

[S5] F. H. Liu, B. Y. Zhao, W. P. Wu, H. Y. Yang, Y. S. Ning, Y. J. Lai, R. Bradley, Low cost, robust, environmentally friendly geopolymer-mesoporous carbon composites for efficient solar powered steam generation, Adv. Funct. Mater. 28 (2018) 1803266.

[S6] Y. Ito, Y. Tanabe, J. Han, T. Fujita, K. Tanigaki, M. Chen, Multifunctional porous graphene for high-efficiency steam generation by heat localization, Adv. Mater. 27 (2015) 4302-4307.

[S7] X. Li, W. Xu, M. Tang, L. Zhou, B. Zhu, S. Zhu, J. Zhu, Graphene oxide-based efficient and scalable solar desalination under one sun with a confined 2D water path, P. Natl. Acad. Sci. U.S.A. 113 (2016) 13953-13958.

[S8] H. Liu, C. Chen, G. Chen, Y. Kuang, X. Zhao, J. Song, C. Jia, X. Xu, E. Hitz, H. Xie, S. Wang, F. Jiang, T. Li, Y. Li, A. Gong, R. Yang, S. Das, L. Hu, High-performance solar steam device with layered channels: Artificial tree with a reversed design, Adv. Energy Mater. 8 (2018) 1701616.

[S9] G. Xue, K. Liu, Q. Chen, P. Yang, J. Li, T. Ding, J. Duan, B. Qi, J. Zhou, Robust and low-cost flame-treated wood for high-performance solar steam generation, ACS Appl. Mater. Interfaces 9 (2017) 15052-15057.

[S10] S. Ma, C. P. Chiu, Y. Zhu, C. Y. Tang, H. Long, W. Qarony, X. Zhao, X. Zhang, W. H. Lo, Y. H. Tsang, Recycled waste black polyurethane sponges for solar vapor generation and distillation, Appl. Energy 206 (2017) 63-69.

[S11] C. Chen, Y. Li, J. Song, Z. Yang, Y. Kuang, E. Hitz, C. Jia, A. Gong, F. Jiang, J. Y. Zhu, B. Yang, J. Xie, L. Hu, Highly flexible and efficient solar steam generation device, Adv. Mater. 29 (2017) 1701756.

[S12] G. Wang, Y. Fu, X. Ma, W. Pi, D. Liu, X. Wang, Reusable reduced graphene oxide based double-layer system modified by polyethylenimine for solar steam generation, Carbon 114 (2017) 117-124.

[S13] Y. Yang, R. Zhao, T. Zhang, K. Zhao, P. Xiao, Y. Ma, P. M. Ajayan, G. Shi, Y. Chen, Graphene-based standalone solar energy converter for water desalination and purification, ACS Nano 12 (2018) 829-835.

[S14] J. Yang, Y. Pang, W. Huang, S. K. Shaw, J. Schiffbauer, M. A. Pillers, X. Mu, S. Luo, T. Zhang, Y. Huang, G. Li, S. Ptasinska, M. Lieberman, T. Luo, Functionalized graphene enables highly efficient solar thermal steam generation, ACS Nano 11 (2017) 5510-5518.

[S15] X. Wang, Q. Liu, S. Wu, B. Xu, H. Xu, Multilayer polypyrrole nanosheets with self-organized surface structures for flexible and efficient solar-thermal energy conversion, Adv. Mater. 31 (2019) 1807716.

[S16] L. Zhang, B. Tang, J. Wu, R. Li, P. Wang, Hydrophobic light-to-heat conversion membranes with self-healing ability for interfacial solar heating, Adv. Mater. 27 (2015) 4889-4894.

[S17] Y. Zhang, X. Yin, B. Yu, X. Wang, Q. Guo, J. Yang, Recyclable polydopamine-functionalized sponge for high-efficiency clean water generation with dual-purpose solar evaporation and contaminant adsorption. ACS Appl. Mater. Interfaces 11(35) (2019) 32559-32568.

[S18] S. Meng, X. Zhao, C.-Y. Tang, P. Yu, R.-Y. Bao, Z.-Y. Liu, M.-B. Yang, W. Yang, A bridge-arched and layer-structured hollow melamine foam/reduced graphene oxide composite with an enlarged evaporation area and superior thermal insulation for high-performance solar steam generation, J. Mater. Chem. A 8 (2020) 2701-2711.

[S19] Y. Shao, Z. Jiang, Y. Zhang, T. Wang, P. Zhao, Z. Zhang, J. Yuan, H. Wang, All-poly(ionic liquid) membrane-derived porous carbon membranes: Scalable synthesis and application for photothermal conversion in seawater desalination, ACS Nano 12 (2018) 11704-11710.

[S20] M. Spinner, A. Kovalev, S. N. Gorb, G. Westhoff, Snake velvet black: Hierarchical micro and nanostructure enhances dark colouration in Bitis rhinoceros, Sci. Rep. 3(1) (2013) 1846.

